

X-type electrides hosting skin-like interstitial electron states and doping-enhanced superconductivity

Da-Bao Zha,¹ Peng Jiang ^{1,*} Yan-Ling Li ^{1,†} and Hai-Qing Lin^{2,‡}

¹Laboratory for Quantum Design of Functional Materials,

and School of Physics and Electronic Engineering, Jiangsu Normal University, Xuzhou 221116, China

²Institute for Advanced Study in Physics and School of Physics, Zhejiang University, Hangzhou 310058, China

The exploration of electrides is of great significance for the fundamental physics due to their unique properties arising from interstitial anionic electrons. Here we report a novel class of X-type electrides, distinguished by two distinct anionic electron subchannels forming alternating chains in real space. Through structural symmetry analysis and first-principles calculations, we identify two-dimensional M_2N ($M = \text{Ti, Zr, Hf}$) materials as prototypical systems exhibiting these unique features. The anionic electron channels on the upper and lower surfaces of these materials display a vertically alternating pattern, with their projected bands revealing momentum-dependent splitting behavior in the reciprocal space, protected by a crystal symmetry operation O . Notably, the X-type electride characteristic is independent of the layer number and remains robust on the upper and lower surfaces of layered structures, presenting a pronounced skin-like effect. Additionally, we have explored the superconductivity of these systems, and found that both Ti_2N and Zr_2N are intrinsic superconductors with superconducting transition temperatures below 1.0 K. Further results show that appropriate hole doping can significantly enhance their superconducting transition temperatures and can induce the Hf_2N monolayer to exhibit superconductivity. Our findings provide valuable insights into the design and tuning of novel electrides with enhanced superconducting properties, offering a new pathway for deeply understanding the interplay between electride behavior and superconductivity in novel materials.

I. INTRODUCTION

Anisotropy in condensed matter systems is critical in determining physical properties and has attracted significant attention due to its impact on magnetism [1–4], electronic transport [5, 6], and optical behavior [7, 8]. It arises from the breaking of certain symmetries, including time-reversal and spatial inversions, and translation operations, which are often associated with various types of ordering, such as, the atom or lattice arrangement [5, 9], spin alignment [10–12], and charge distribution [13–15], etc. Moreover, the interactions between these ordering parameters in the system can lead to the emergence of distinct singularities, facilitating the discovery of novel and complex physical properties. A prominent example is altermagnetism or X-type antiferromagnet [3, 4, 12], a novel magnetic phase where momentum-dependent spin splitting without spin-orbital coupling emerges as a direct consequence of the intricate coupling between spin order and lattice order. Such an example underscores the importance of investigating the coupling between these ordering parameters, as it not only enhances our understanding of fundamental physical phenomena but also provides critical insights for the discovery of novel material properties.

Beyond these magnetic states, electrides [15–19], where excess valence electrons are confined to interstitial spaces in a positively charged crystalline framework and behave as anions, constitute an unconventional class of compounds. The presence of highly mobile non-nucleus-bound electrons in electrides endows them with immense potential for applications in optoelectronics and catalysis [20, 21]. Based on the

connectivity of crystal cavities and channels, as well as the dimensionality of interstitial electron distribution and its coupling with the lattice arrangement, electrides can be categorized as zero-, one-, and two-dimensional (0D, 1D, and 2D) phases [22–25]. In particular, when the interstitial electron distribution behaves as a 1D electron gas, lying between 0D and 2D configurations, it often gives rise to novel physical phenomena, such as superconductivity [26, 27], and nontrivial topological states [20, 28], due to the restriction of electron motion in a specific direction. Furthermore, the quantum confinement effect enhances the density of electronic states near the Fermi level, which can induce Stoner-type instability and promote the formation of a magnetic state [29, 30]. In this case, the 1D electrides can serve as an idea platform to explore the connection between electronic anisotropy and lattice structure and also uncovers the fundamental mechanisms governing physical properties. It should be emphasized that, in a conventional 1D electride shown in Fig. 1(a), the interstitial anionic electron (IAE) channels are periodically aligned parallel to the nearest neighbors, dictated by the translational symmetry of the system. A natural question is raised: when the IAE channel is regarded as a degree of freedom (analogous to a pseudospin), could electrides exhibit a X-type antiferromagnetic-like state, characterized by a new arrangement where two distinct IAE subchannels are parallel within the same plane but alternate in a crossing pattern between adjacent planes [see Fig. 1(b)]? Due to the crossing of these IAE channels in electrides with such a stacking order, we refer to them as cross-chain or X-type electrides. If such a state were realized, these IAE states might not only exhibit anisotropy in real space but also display distinct signatures in momentum space. Additionally, numerous studies have shown that electrides provide a great platform for studying superconductivity, yet the role of these anisotropic anionic electron states in superconductivity has not been fully revealed.

* pjiang@jsnu.edu.cn; pjiang93@mail.ustc.edu.cn

† ylli@jsnu.edu.cn

‡ hqlin@zju.edu.cn

In this work, we propose a new class of thermodynamically and dynamically stable *X*-type electrides, exemplified by the 2D M_2N ($M = \text{Ti, Zr and Hf}$) systems. Electronic structure analysis reveals that 1D IAE subchannels are anisotropically distributed across the upper and lower surfaces, forming a vertically alternating pattern in the real space. This unique characteristic leads to distinguishable momentum-dependent bands for the two anionic electron subchannels, highlighting their anisotropic distribution and the significant influence of lattice symmetry. In addition, the Ti_2N and Zr_2N monolayers are shown to be intrinsic superconductors with T_c values of 0.8 K and 0.6 K, respectively. Remarkably, the T_c of the Ti_2N monolayer can be enhanced to 3.2 K under a doping concentration of 0.6 hole/f.u., and the Hf_2N monolayer exhibits a superconducting state under an appropriate hole doping, providing insights into the suppressive effect of anionic electrons in electrides on superconductivity.

II. COMPUTATIONAL METHODS AND DETAILS

The calculations for structural and electronic properties of the M_2N ($M = \text{Ti, Zr and Hf}$) monolayers are carried out using the Vienna Ab-initio Simulation Package (VASP) package [31, 32], which is based on density functional theory (DFT) within projector augmented wave (PAW) method [33]. The generalized gradient approximation with the Perdew-Burke-Ernzerhof (PBE) functional is used to describe the exchange-correlation term [34]. The cut-off energy of the plane wave is set to 500 eV. All crystal structures are relaxed until the forces per atom are less than 1 meV/Å and total energies are converged to 10^{-6} eV. The k -mesh grids of $14 \times 14 \times 1$ and $14 \times 14 \times 10$ are sampled in the Brillouin zone (BZ) by using the Monkhorst-Pack scheme in the monolayer and bulk M_2N systems, respectively. The electron localization function (ELF) is used to analyse the inter-atomic bonding [35]. The phonon spectra and electron-phonon coupling (EPC) calculations are performed using the density functional perturbation theory (DFPT), as implemented in the QUANTUM ESPRESSO package [36], in which the k -mesh and q -mesh are both set to $8 \times 8 \times 1$. The electronic states are described using optimized norm-conserving Vanderbilt (ONCV) pseudopotentials [37], with cutoff energies of 90 Ry for the wave function and 450 Ry for the charge density. The superconducting T_c is calculated by using the McMillan-Allen-Dynes formula [38], namely, $T_c = \frac{\omega_{\text{log}}}{1.2} \exp\left[-\frac{1.04(1+\lambda)}{\lambda - \mu^*(1+0.62\lambda)}\right]$, where a typical value of 0.11 for the effective Coulomb repulsion parameter μ^* is adopted [39].

III. RESULTS AND DISCUSSION

Characteristics and Stability. The optimized structures of the monolayer transition metal nitrides M_2N ($M = \text{Ti, Zr and Hf}$) are presented in Figs. 1(c) and 1(d). Similar to 2D SnO_2 [40], the M_2N monolayers hold a tetrahedral lattice with a buckled geometrical configuration consisting of MN_4 tetra-

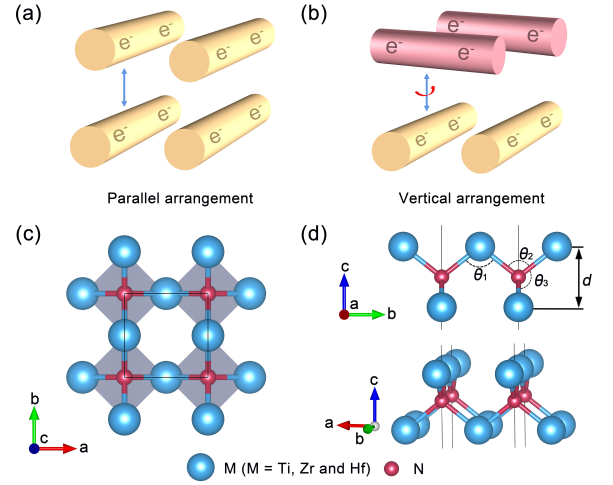


FIG. 1. (a) Conventional 1D electride with the parallel-aligned interstitial anionic electron subchannels. (b) Novel *X*-type electrides characterized by alternating interstitial anionic electron subchannels that are aligned parallel within the same plane but intersect in adjacent planes. (c) Top and (d) side views of the crystal structures of the M_2N monolayers.

hedron. As shown in Figs. 1(d), M - N - M - N - M atoms in the M_2N monolayers form an open dome-shaped channel along the x and y directions, respectively. These two open channels can be connected by S_{4z} operation since the M_2N monolayers belong to $P\bar{4}m2$ (No. 115) space group with D_{2d} point symmetry. Note that all M_2N systems share similar crystal structures and electronic band characteristics (as discussed below), we thus primarily focus on Ti_2N as a representative example in the following analysis. We perform density functional theory calculations and find that the in-plane lattice constants are $a = b = 2.99$ Å. Other structural parameters are summarized in Table S1 of the Supplementary Information.

To evaluate the energetic stability of the Ti_2N monolayer, we calculate its formation energy defined as $E_{\text{for}} = (E_{\text{Ti}_2\text{N}} - 2E_{\text{Ti}} - E_{\text{N}})/3$, where $E_{\text{Ti}_2\text{N}}$ is the total energy of the Ti_2N monolayer; E_{Ti} and E_{N} represent the atomic chemical potentials derived from their respective stable phases under ambient conditions. The calculated E_{for} is about -0.38 eV/atom, indicating that the monolayer is energetically favorable for experimental synthesis. The phonon dispersion is then calculated and the absence of imaginary frequencies confirms the dynamical stability of the Ti_2N monolayer (see Fig. S1 of the Supplementary Information). Moreover, the thermal stability is assessed via *ab-initio* molecular dynamics simulations (see Fig. S2 of the Supplementary Information). The results indicate that the Ti_2N monolayer exhibits robust thermal stability, with stable energy fluctuations and no significant structural reconstruction.

Momentum-dependent interstitial anionic electron distribution. To further reveal the electronic properties of the Ti_2N monolayer, we analyze its electronic band structure and the corresponding projected density of states (PDOS). As shown in Fig. 2, there are two hole-like bands and one electron-like band crossing the Fermi level, with no inter-

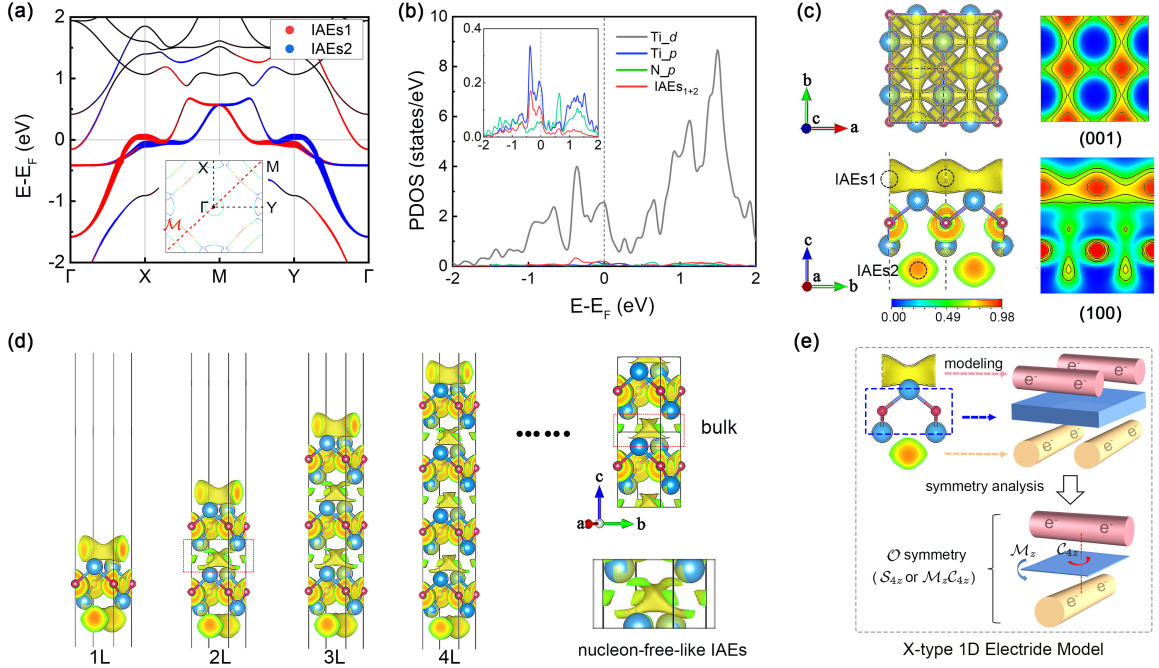


FIG. 2. (a) IAE-projected band structure of the Ti_2N monolayer, and the inset shows the Fermi surface in the first BZ. (b) PDOS of the Ti_2N monolayer, the inset displays the enlarged view of the contribution of interstitial electrons around the Fermi level. (c) Different views of the ELF maps with the isosurface values of 0.55. The black dashed circles denote the position of pseudoatoms. (d) ELF of 1-, 2-, 3-, 4-layer and bulk Ti_2N structures. (e) The symmetry analysis of the X-type 1D electrode model, where the cylinder and cuboid represents IAEs and 2D atomic layer, respectively.

sections between them (see the inset in Fig. 2(a)), indicating the semi-metallic characteristic of the Ti_2N monolayer. The PDOS shown in Fig. 2(b) demonstrates that these bands are predominantly derived from Ti- d orbitals, while contributions from Ti- p and N- p orbitals are minimal.

Given that the usual valence states of Ti (Ti^{2+} , Ti^{3+} , or Ti^{4+}) in the nitrides or oxides and N (N^{3-}) in the metal nitrides, it is naturally expected that the system may possess excess electrons, behaving as IAEs. This electronic behaviour can be confirmed by the ELF that is usually used to characterize the bonding feature [41], and the corresponding results are displayed in Figs. 2(c). We can see that two distinct excess electronic states are loosely confined to the dome-shaped interstitial spaces above and below the atomic layers, with the upper and lower IAEs labelled as IAE1 and IAE2, respectively. Notably, both IAE1 and IAE2 form continuous 1D electronic states with spatially orthogonal and separated distributions, leading to an alternating electronic configuration in real space. To examine the layer-dependent distribution of IAEs, ELF calculations for 1-, 2-, 3-layer, 4-layer, and bulk Ti_2N are conducted [see Fig. 2(d)]. It is indicated that the alternating IAE configuration persists in multi-layered systems and remains spatially and perpendicularly separated on the upper and lower surfaces of 2D layered materials. Moreover, the momentum-dependent IAE characteristics persist in the band structures of multilayer systems (see Fig. S3 of the Supplementary Information), manifesting a skin-like distribution of IAEs at the top and bottom surfaces. This surface-

confinement behavior, which we term a “skin-like effect”, is first reported here in electrides. It is important to note that this phenomenon differs fundamentally from the classical skin effect in conductors [42], which arises from electromagnetic induction and frequency-dependent current distribution. In contrast, the skin-like effect observed here originates from quantum confinement and the symmetry-protected localization of IAEs. In addition, the multilayer Ti_2N exhibits a nucleon-free-like IAE behavior between its layers, akin to the bulk Ti_2N electride.

In order to estimate the number of interstitial electrons in the Ti_2N monolayer, we have performed a Bader charge analysis, which reveals that the Bader charges of Ti, N, and IAEs are 1.77 |e|, -1.53 |e|, and -2.00 |e|, respectively. These indicate that interstitial charges function as anionic electrons and are primarily derived from Ti atoms. Combined with the above results, the chemical formula of the Ti_2N electride can be expressed as $(\text{Ti}_2\text{N})^{2+} \cdot 2e^-$. Additionally, we employ the widely-used pseudoatom method to calculate the IAE-projected band structure and PDOS [43, 44], as shown in Figs. 2(a) and 2(b). It is shown that IAE1 and IAE2 exhibit a distinct energy-splitting feature, and are related by a diagonal mirror symmetry \mathcal{M} in the momentum (\mathbf{k}) space, similar to previously reported spin-split band structures for altermagnetic and X-type antiferromagnetic phases [3, 4, 12, 45].

Next, we analyse symmetry conditions for the distinguishable behaviour of \mathbf{k} -dependent IAE distribution. Without loss of generality, we consider the Ti_2N system with two sub-

lattices: the top sublattice with $z > 0$ and the bottom one with $z < 0$, in which $z = 0$ corresponds to the N atomic layer (see Fig. 2(e)). By definition, the electron charge of the top/bottom sublattice can be expressed simply as $\rho_{1/2} = e \sum_n \int_{\Omega} \int_{z>0/z<0} f_{nk} \langle \psi_{nk} | \psi_{nk} \rangle d\mathbf{r} d\mathbf{k} = \int_{\Omega} \rho_{1/2}(\mathbf{k}) d\mathbf{k}$, in which the numbers 1 and 2 denote the layer index for convenience; e is the electron charge; f_{nk} is the Fermi-Dirac distribution function; n is the band index for the occupied states; $\mathbf{k} = (k_x, k_y)$ indicate the momentum in the 2D BZ. Under the O symmetry operation, \mathbf{k} should be changed to $\mathbf{k}' = (k_y, k_x)$, namely, $O\mathbf{k} = \mathbf{k}'$. It is clear that ρ_1 and ρ_2 can be connected by O operation (S_{4z} or $C_{4z}M_z$) from the structural symmetry (see Fig. 2(e)), that is, $O^\dagger \rho_1 O = \rho_2$. Thus, one can get

$$\begin{aligned} O^\dagger \varepsilon_{1n}(\mathbf{k}) O &= O^\dagger \int_{z>0} \langle \psi_{n\mathbf{k}}(\mathbf{r}) | \hat{H}_1 | \psi_{n\mathbf{k}}(\mathbf{r}) \rangle d\mathbf{k} O \\ &= \int_{z<0} \langle \psi_{nO\mathbf{k}}(\mathbf{r}) | \hat{H}_2 | \psi_{nO\mathbf{k}}(\mathbf{r}) \rangle d\mathbf{r} = \varepsilon_{2n}(\mathbf{k}'). \end{aligned} \quad (1)$$

Meanwhile, the broken M_z symmetry in the M_2N structures can guarantee that $\varepsilon_{1n}(\mathbf{k}) \neq \varepsilon_{2n}(\mathbf{k})$ is occurred, meaning that the energy distributions of IAE1 and IAE2 are always degenerate at same \mathbf{k} path but are symmetric through the diagonal mirror symmetry of 2D BZ.

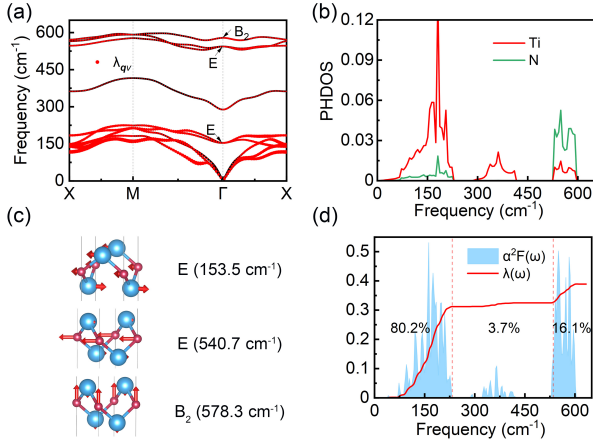


FIG. 3. (a) Phonon spectrum with the EPC strength λ_{qv} for each phonon mode and (b) atomic projected PHDOS of the Ti_2N monolayer. The size of dots is proportional to the λ_{qv} strength. (c) Eigenvectors of the infrared and Raman (I+R) active modes at the Γ point. (d) Eliashberg spectral function $\alpha^2F(\omega)$, represented by the shaded area, and the cumulative frequency-dependent EPC constant $\lambda(\omega)$ represented by the red line of the Ti_2N monolayer.

Enhanced superconducting properties by the hole-doping. To gain a deeper understanding into EPC properties of the Ti_2N monolayer, the phonon spectrum with the EPC strength for each phonon mode λ_{qv} , atomic projected phonon DOS (PHDOS), and Eliashberg spectral function $\alpha^2F(\omega)$ are calculated and the results are shown in Fig. 3. From the phonon spectrum and PHDOS present in Figs. 3(a-b), we can find that the main contribution to the EPC strength attributes to the low-frequency phonon modes below 250 cm^{-1} , which are primarily associated with the stretching vibrations between Ti

and N atoms in the infrared and Raman E modes [see the vibration pattern at a frequency of 153.5 cm^{-1} in Fig. 3(c)]. These low-frequency vibrations contributes 80.2% of the total EPC strength, as shown in Fig. 3(d). Furthermore, the high-frequency phonon modes above 500 cm^{-1} mainly originate from the in-plane and out-of-plane vibrations of N atoms, which contributes 16.1% of the total EPC strength. In contrast, the intermediate-frequency phonon modes between 250 and 500 cm^{-1} make a negligible contribution. Therefore, the main contribution to the EPC strength is from Ti vibrations. Using the McMillan-Allen-Dynes formula [38], the superconducting T_c of the Ti_2N monolayer is estimated to be around 0.8 K . We have also analyzed the superconductivity of the bulk Ti_2N and found its T_c to be 5.5 K , significantly higher than that of the Ti_2N monolayer. The increase of T_c is closely to the delocalization of IAEs with increasing layer number.

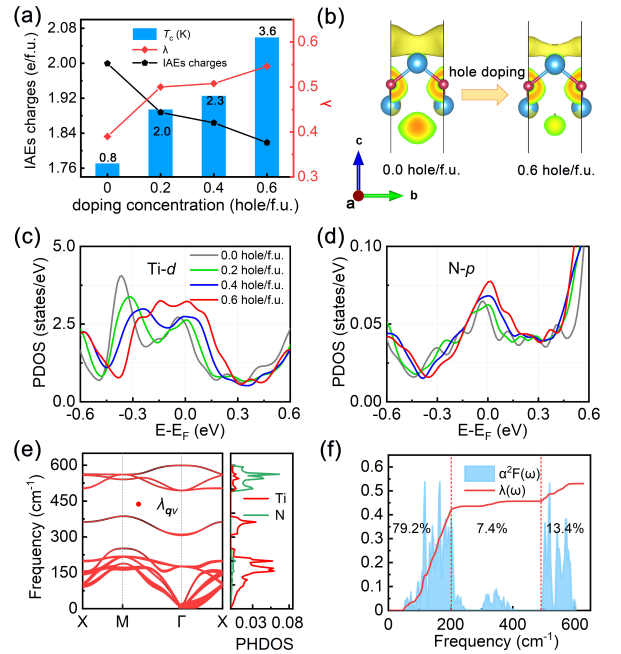


FIG. 4. (a) Hole doping concentration (n_h) dependent T_c and λ in the Ti_2N monolayer. (b) ELF evolution from $n_h = 0.0$ hole/f.u. to $n_h = 0.6$ hole/f.u.. (c) Ti- d and (d) N- p orbitals PDOS at different n_h . (e) Phonon spectrum with the γ_{qv} attached, atom projected PHDOS, and (f) Eliashberg spectral function $\alpha^2F(\omega)$ and cumulative frequency-dependent EPC constant of the Ti_2N monolayer at $n_h = 0.6$ hole/f.u..

To investigate the influence of changes in IAEs on the electronic structure of $(\text{Ti}_2\text{N})^{2+} \cdot 2e^-$, we introduce hole carriers to neutralize anionic electrons, thereby modulating the electronic structure. Firstly, the T_c at different doping concentrations of hole carriers (n_h) is examined, as depicted in Fig. 4(a). With increasing n_h , a significant rise in the T_c is observed. More specifically, hole doping increases the EPC strength from $\lambda = 0.39$ in the undoped case to $\lambda = 0.55$ at $n_h = 0.6$ hole/f.u. It is well-known that the T_c is closely related to λ and the logarithmical averaged frequency ω_{\log} . Note that, although ω_{\log} is decreased with increasing n_h , the enhancement of λ dominates an increase in the T_c . When n_h reaches

0.6 hole/f.u., the T_c rises from 0.8 K in the pristine case to 3.2 K. Although the T_c remains relatively low at moderate hole doping concentration, it increases fourfold compared to the undoped case, which can be attributed to the neutralization of anionic electrons. This trend is clearly confirmed by the ELF shown in Fig. 4(b). It is found that the spatial distribution of IAEs becomes more confined, indicating that the number of IAEs decreases with increasing n_h . Consequently, the Bader charge of IAEs decreases from -2.00 |e| to -1.80 |e| when n_h increases from 0.0 hole/f.u. to 0.6 hole/f.u.

As illustrated in Figs. 4(c) and 4(d), a gradual reduction in the number of IAEs on the surface leads to an increase in delocalized electrons near the Fermi surface, predominantly originating from Ti- d and N- p orbitals. From the electronic perspective, the increase of the doping concentration reduces the Coulomb attraction between IAEs and the host cationic lattice, facilitating Cooper pair formation and enhancing superconducting properties [46]. In this context, we investigate the effect of hole doping on phononic properties, using the representative case of 0.6 hole/f.u. as an example. The phonon dispersion with the attached λ_{qv} and atomic-projected PHDOS for the Ti_2N monolayer at 0.6 hole/f.u. are shown in Fig. 4(e). Similar to the undoped case, the high-frequency region exhibits significant phonon linewidth contributions, primarily associated with the vibrations of N atoms. Meanwhile, Fig. 4(f) reveals an increase in the proportion of λ in the low- and intermediate-frequency regions. From the above results, it can be concluded that hole doping induces two key effects: first, the reduction in the number of excess electrons enhances the density of delocalized electrons near the Fermi surface; second, the weakening of Coulomb interactions between IAEs and host cations facilitates favorable vibrations of Ti atoms in the low- and intermediate-frequency regions of phonons, thereby increasing their contribution to superconductivity.

Considering that Zr and Hf belong to the same group as titanium, we substituted Ti atoms in Ti_2N with Zr and Hf, resulting in Zr_2N and Hf_2N systems, both of which are dynamically stable (see Fig. S1 of the Supplementary Information). Their electronic structures were subsequently analyzed, as shown in Fig. S4 of the Supplementary Information, revealing that Zr_2N and Hf_2N monolayers exhibit X-type 1D electrider features. This behavior can be attributed to their identical crystal structure to Ti_2N and the shared valence state of Zr and Hf. Furthermore, the superconducting properties of Zr_2N and Hf_2N monolayers are investigated, with results presented in Fig. S5 of the Supplementary Information. It is found that the Zr_2N monolayer is an intrinsic superconductor with a T_c of 0.6 K in the undoped state, while the Hf_2N monolayer

shows no superconductivity. Interestingly, with hole doping, both of two systems demonstrate enhanced superconducting behavior. The T_c of the Zr_2N monolayer is increased significantly with higher doping concentrations. Moreover, the Hf_2N monolayer exhibits a superconducting state under the hole doping, and its T_c continues to rise with creasing doping concentration. These findings support the conclusion that the introduction of the holes in the X-type electrider $M_2\text{N}$ system can effectively enhance their superconductivity by strengthening the Coulomb interaction between delocalized IAEs and host cations.

IV. CONCLUSION

In summary, we have proposed a novel class of X-type 1D electrideres, which is verified by the predicted 2D $M_2\text{N}$ ($M = \text{Ti}, \text{Zr}, \text{and Hf}$) systems. These materials exhibit unique anisotropic IAE distributions, forming vertically alternating 1D chains along the superficial channels. The symmetry analysis reveals that these distinguishable IAE subchannels on the upper and lower surfaces can be reflected in momentum-dependent subchannel-splitting band. It is noteworthy that the X-type electrider characteristic is preserved independently of the number of layers due to the imposed S_{4z} symmetry of the atomic arrangement, manifesting as a skin-like effect. Importantly, Ti_2N and Zr_2N monolayers are found to be intrinsic superconductors, with lower superconducting T_c , respectively. Furthermore, the hole doping is demonstrated to enhance the EPC and T_c in these electrideres, driven by an increase in electronic states near the Fermi level and a strengthened interaction between the host cations and delocalized IAEs. Our findings not only report the first X-type 1D electrideres with superconductivity, but also demonstrate the significant role of the coupling of lattice and charge orderings between in shaping the physical properties in electrideres, offering a new platform to explore the interaction between electrider state and superconductivity.

V. ACKNOWLEDGMENTS

We acknowledge support from the National Natural Science Foundation of China (Grants No. 12204202 and No. 12074153), the Natural Science Foundation of Jiangsu Province (Grant No. BK20220679), and the Natural Science Fund for Colleges and Universities in Jiangsu Province (Grant No. 22KJB140010).

-
- [1] W. H. Meiklejohn and C. P. Bean, New Magnetic Anisotropy, *Phys. Rev.* **105**, 904 (1957).
 - [2] B. Dieny and M. Chshiev, Perpendicular magnetic anisotropy at transition metal/oxide interfaces and applications, *Rev. Mod. Phys.* **89**, 025008 (2017).
 - [3] L. Šmejkal, J. Sinova, and T. Jungwirth, Beyond conventional ferromagnetism and antiferromagnetism: A phase

with nonrelativistic spin and crystal rotation symmetry, *Phys. Rev. X* **12**, 031042 (2022).

- [4] L. Šmejkal, J. Sinova, and T. Jungwirth, Emerging research landscape of altermagnetism, *Phys. Rev. X* **12**, 040501 (2022).
- [5] J. Qiao, X. Kong, Z.-X. Hu, F. Yang, and W. Ji, High-mobility transport anisotropy and linear dichroism in few-layer black phosphorus, *Nat. Commun.* **5**, 4475 (2014).

- [6] C. Liu, X. Yan, D. Jin, Y. Ma, H.-W. Hsiao, Y. Lin, T. M. Bretz-Sullivan, X. Zhou, J. Pearson, B. Fisher, J. S. Jiang, W. Han, J.-M. Zuo, J. Wen, D. D. Fong, J. Sun, H. Zhou, and A. Bhattacharya, Two-dimensional superconductivity and anisotropic transport at KTaO_3 (111) interfaces, *Science* **371**, 716 (2021).
- [7] H. Wang, Q. Chen, Y. Cao, W. Sang, F. Tan, H. Li, T. Wang, Y. Gan, D. Xiang, and T. Liu, Anisotropic strain-tailoring nonlinear optical response in van der Waals NbOI_2 , *Nano Lett.* **24**, 3413 (2024).
- [8] S. Huang, Y. Tatsumi, X. Ling, H. Guo, Z. Wang, G. Watson, A. A. Puzetzy, D. B. Geohegan, J. Kong, J. Li, T. Yang, R. Saito, and M. S. Dresselhaus, In-plane optical anisotropy of layered gallium telluride, *ACS Nano* **10**, 8964 (2016).
- [9] J. Zhao, D. Ma, C. Wang, Z. Guo, B. Zhang, J. Li, G. Nie, N. Xie, and H. Zhang, Recent advances in anisotropic two-dimensional materials and device applications, *Nano Res.* **14**, 897 (2021).
- [10] J. L. Lado and J. Fernández-Rossier, On the origin of magnetic anisotropy in two dimensional CrI_3 , *2D Mater.* **4**, 035002 (2017).
- [11] W. Wang, M. W. Daniels, Z. Liao, Y. Zhao, J. Wang, G. Koster, G. Rijnders, C.-Z. Chang, D. Xiao, and W. Wu, Spin chirality fluctuation in two-dimensional ferromagnets with perpendicular magnetic anisotropy, *Nat. Mater.* **18**, 1054 (2019).
- [12] S.-S. Zhang, Z.-A. Wang, B. Li, Y.-Y. Jiang, S.-H. Zhang, R.-C. Xiao, L.-X. Liu, X. Luo, W.-J. Lu, M. Tian, Y.-P. Sun, E. Y. Tsymlal, H. Du, and D.-F. Shao, X-type stacking in cross-chain antiferromagnets, *Newton* **1**, 100068 (2025).
- [13] G. Grüner, The dynamics of charge-density waves, *Rev. Mod. Phys.* **60**, 1129 (1988).
- [14] B. Kiraly, E. J. Knol, K. Volckaert, D. Biswas, A. N. Rudenko, D. A. Prishchenko, V. G. Mazurenko, M. I. Katsnelson, P. Hofmann, D. Wegner, and A. A. Khajetoorians, Anisotropic Two-Dimensional Screening at the Surface of Black Phosphorus, *Phys. Rev. Lett.* **123**, 216403 (2019).
- [15] J. L. Dye, Electrons as anions, *Science* **301**, 607 (2003).
- [16] X. Yang, K. Parrish, Y.-L. Li, B. Sa, H. Zhan, and Q. Zhu, Switchable two-dimensional electrides: A first-principles study, *Phys. Rev. B* **103**, 125103 (2021).
- [17] Z. Liu, Q. Zhuang, F. Tian, D. Duan, H. Song, Z. Zhang, F. Li, H. Li, D. Li, and T. Cui, Proposed superconducting electride Li_6C by sp -hybridized cage states at moderate pressures, *Phys. Rev. Lett.* **127**, 157002 (2021).
- [18] Z. Zhao, S. Zhang, T. Yu, H. Xu, A. Bergara, and G. Yang, Predicted pressure-induced superconducting transition in electride Li_6P , *Phys. Rev. Lett.* **122**, 097002 (2019).
- [19] X. Wang, Y. Wang, J. Wang, S. Pan, Q. Lu, H.-T. Wang, D. Xing, and J. Sun, Pressure stabilized lithium-aluminum compounds with both superconducting and superionic behaviors, *Phys. Rev. Lett.* **129**, 246403 (2022).
- [20] J. Wang, X. Sui, S. Gao, W. Duan, F. Liu, and B. Huang, Anomalous Dirac plasmons in 1D topological electrides, *Phys. Rev. Lett.* **123**, 206402 (2019).
- [21] T.-N. Ye, Y. Lu, J. Li, T. Nakao, H. Yang, T. Tada, M. Kitano, and H. Hosono, Copper-based intermetallic electride catalyst for chemoselective hydrogenation reactions, *J. Am. Chem. Soc.* **139**, 17089 (2017).
- [22] K. Lee, S. W. Kim, Y. Toda, S. Matsuishi, and H. Hosono, Dicalcium nitride as a two-dimensional electride with an anionic electron layer, *Nature* **494**, 336 (2013).
- [23] T. Inoshita, S. Jeong, N. Hamada, and H. Hosono, Exploration for two-dimensional electrides via database screening and ab initio calculation, *Phys. Rev. X* **4**, 031023 (2014).
- [24] Z. Li, J. Yang, J. Hou, and Q. Zhu, Inorganic electride: theoretical study on structural and electronic properties, *J. Am. Chem. Soc.* **125**, 6050 (2003).
- [25] W. Ming, M. Yoon, M.-H. Du, K. Lee, and S. W. Kim, First-principles prediction of thermodynamically stable two-dimensional electrides, *J. Am. Chem. Soc.* **138**, 15336 (2016).
- [26] Y. Zhang, B. Wang, Z. Xiao, Y. Lu, T. Kamiya, Y. Uwatoko, H. Kageyama, and H. Hosono, Electride and superconductivity behaviors in Mn_5Si_3 -type intermetallics, *npj Quantum Mater.* **2**, 45 (2017).
- [27] B. Sa, R. Xiong, C. Wen, Y.-L. Li, P. Lin, Q. Lin, M. Anpo, and Z. Sun, Electronic anisotropy and superconductivity in one-dimensional electride Ca_3Si , *J. Phys. Chem. C* **124**, 7683 (2020).
- [28] C. Park, S. W. Kim, and M. Yoon, First-principles prediction of new electrides with nontrivial band topology based on one-dimensional building blocks, *Phys. Rev. Lett.* **120**, 026401 (2018).
- [29] X. Sui, J. Wang, and W. Duan, Prediction of stoner-type magnetism in low-dimensional electrides, *J. Phys. Chem. C* **123**, 5003 (2019).
- [30] S. Liu, C. Wang, B. Wang, Y. Jia, and J. Cho, Flat-band ferromagnetism in the quasi-one-dimensional electride Y_2Cl_3 induced by hole doping, *Phys. Rev. B* **110**, 024413 (2024).
- [31] G. Kresse and J. Furthmüller, Efficient iterative schemes for ab initio total-energy calculations using a plane-wave basis set, *Phys. Rev. B* **54**, 11169 (1996).
- [32] G. Kresse and D. Joubert, From ultrasoft pseudopotentials to the projector augmented-wave method, *Phys. Rev. B* **59**, 1758 (1999).
- [33] P. E. Blöchl, Projector augmented-wave method, *Phys. Rev. B* **50**, 17953 (1994).
- [34] J. P. Perdew, K. Burke, and M. Ernzerhof, Generalized Gradient Approximation Made Simple, *Phys. Rev. Lett.* **77**, 3865 (1996).
- [35] A. D. Becke and K. E. Edgecombe, A simple measure of electron localization in atomic and molecular systems, *J. Chem. Phys.* **92**, 5397 (1990).
- [36] P. Giannozzi, S. Baroni, N. Bonini, M. Calandra, R. Car, C. Cavazzoni, D. Ceresoli, G. L. Chiarotti, M. Cococcioni, I. Dabo, A. D. Corso, S. de Gironcoli, S. Fabris, G. Fratesi, R. Gebauer, U. Gerstmann, C. Gougoussis, A. Kokalj, M. Lazzeri, L. Martin-Samos, N. Marzari, F. Mauri, R. Mazzarello, S. Paolini, A. Pasquarello, L. Paulatto, C. Sbraccia, S. Scandolo, G. Sclauzero, A. P. Seitsonen, A. Smogunov, P. Umari, and R. M. Wentzcovitch, Quantum espresso: a modular and open-source software project for quantum simulations of materials, *J. Phys.: Condens. Matter* **21**, 395502 (2009).
- [37] D. R. Hamann, Optimized norm-conserving Vanderbilt pseudopotentials, *Phys. Rev. B* **88**, 085117 (2013).
- [38] P. B. Allen and R. C. Dynes, Transition temperature of strong-coupled superconductors reanalyzed, *Phys. Rev. B* **12**, 905 (1975).
- [39] Y.-L. Li, E. Stavrou, Q. Zhu, S. M. Clarke, Y. Li, and H.-M. Huang, Superconductivity in the van der Waals layered compound PS_2 , *Phys. Rev. B* **99**, 220503 (2019).
- [40] P. Jiang, L. Kang, X. Zheng, Z. Zeng, and S. Sanvito, Computational prediction of a two-dimensional semiconductor SnO_2 with negative Poisson's ratio and tunable magnetism by doping, *Phys. Rev. B* **102**, 195408 (2020).
- [41] P. Jiang, L. Kang, Y.-L. Li, X. Zheng, Z. Zeng, and S. Sanvito, Prediction of the two-dimensional Janus ferrovalley material LaBrI , *Phys. Rev. B* **104**, 035430 (2021).

- [42] P. J. Nahin, *Oliver Heaviside: sage in solitude* (iecc Press New York, 1987).
- [43] M.-S. Miao and R. Hoffmann, High-pressure electrides: the chemical nature of interstitial quasiatoms, *J. Am. Chem. Soc.* **137**, 3631 (2015).
- [44] D.-B. Zha, P. Jiang, H.-M. Huang, and Y.-L. Li, Refined phase diagram and kagome-lattice superconductivity in Mg-Si system, *Phys. Rev. Mater.* **7**, 114805 (2023).
- [45] F.-F. Huang, P. Jiang, X. Zheng, H.-M. Huang, and Y.-L. Li, Emerging two-dimensional half-metal with high Curie temperature and strain-tunable altermagnetism, *Phys. Rev. B* **110**, 174429 (2024).
- [46] Q. Yang, X. Jiang, and J. Zhao, Coexistence of zero-dimensional electride state and superconductivity in AlH_2 monolayer, *Chin. Phys. Lett.* **40**, 107401 (2023).

SUPPLEMENTARY INFORMATION FOR X-TYPE ELECTRIDES HOSTING SKIN-LIKE INTERSTITIAL ELECTRON STATES AND DOPING-ENHANCED SUPERCONDUCTIVITY

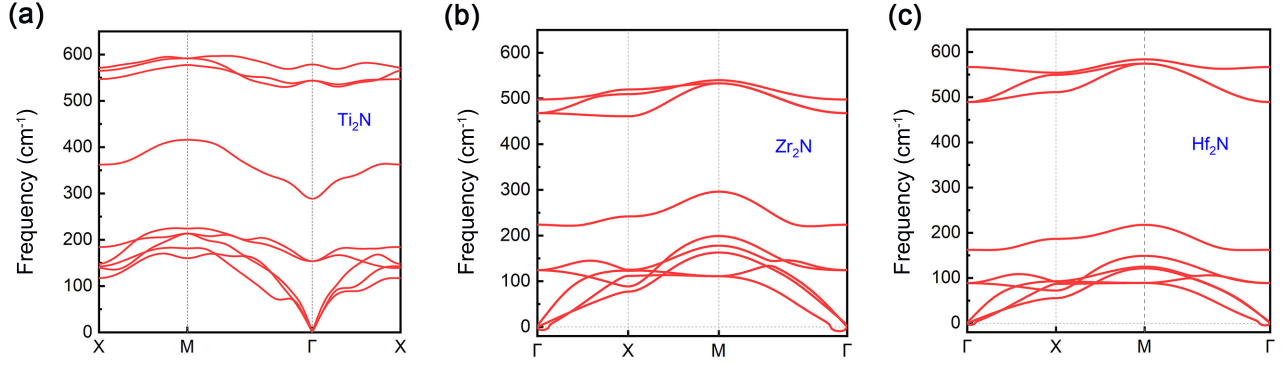


FIG. S1. Phonon spectra of the (a) Ti_2N , (b) Zr_2N , and (c) Hf_2N monolayers, respectively.

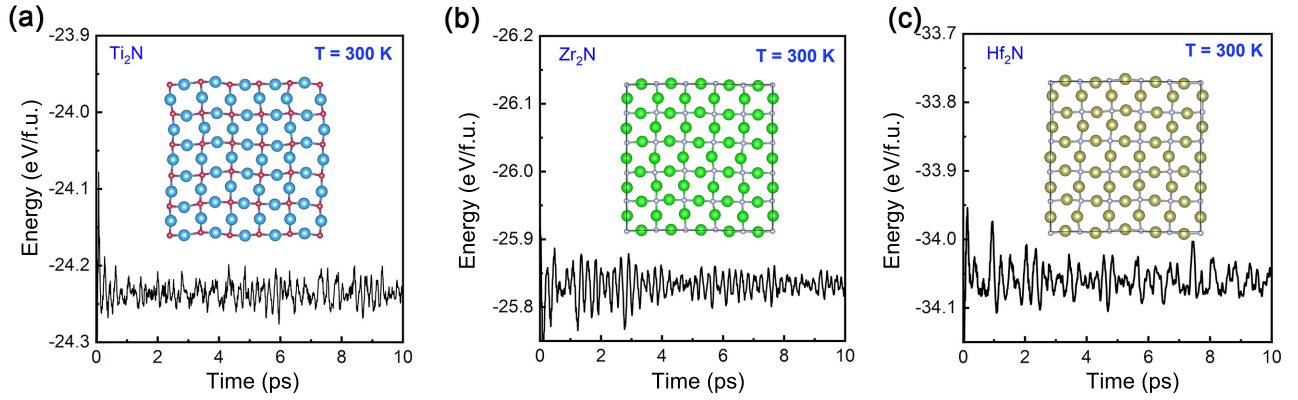


FIG. S2. Total energies (in eV/f.u.) as a function of the simulation time in an *ab-initio* MD simulations at 300 K for the (a) Ti_2N , (b) Zr_2N , and (c) Hf_2N monolayers, respectively.

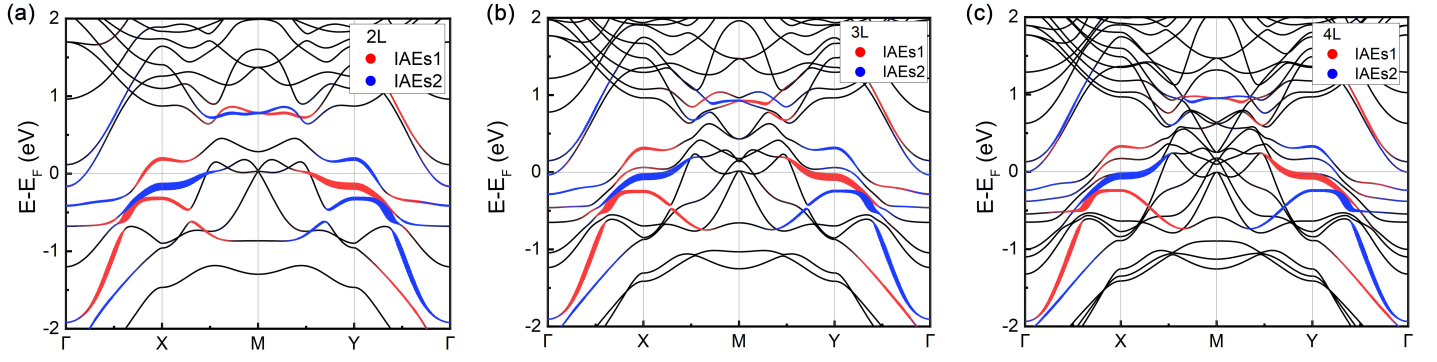


FIG. S3. IAE-projected band structures of the (a) 2-layer, (b) 3-layer, and (c) 4-layer Ti₂N structures.

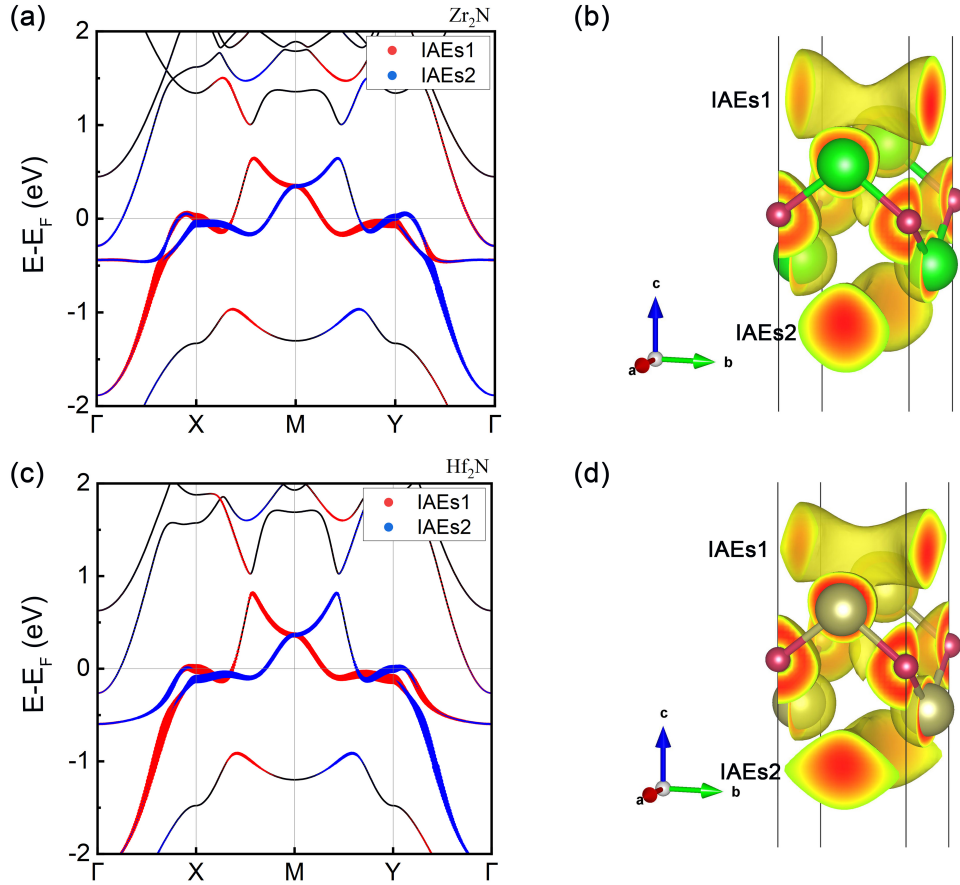


FIG. S4. IAE-projected band structure and ELF maps of the (a-b) Zr₂N and (c-d) Hf₂N monolayers.

TABLE S1. The calculated structural parameters of the M_2N ($M = \text{Ti, Zr and Hf}$) monolayers, in which a , d and d_{M-N} denote the lattice constant, the buckled height, and the M -N bond length, respectively. θ_1 , θ_2 , and θ_3 are the bond angles.

M_2N	d (Å)	d_{M-N} (Å)	bond angles ($^\circ$)			Lattice constants	Wyckoff sites
			θ_1	θ_2	θ_3		
Ti_2N	2.396	1.920	102.70	102.70	112.90	$a = b = 2.998 \text{ Å}$	Ti 2g (0.0000, 0.5000, 0.5398)
						$c = 30 \text{ Å}$	N 1d (0.0000, 0.0000, 0.5000)
Zr_2N	2.561	2.068	103.50	103.50	112.54	$a = b = 3.248 \text{ Å}$	Zr 2g (0.0000, 0.5000, 0.5427)
						$c = 30 \text{ Å}$	N 1d (0.0000, 0.0000, 0.5000)
Hf_2N	2.574	2.052	102.31	102.31	113.17	$a = b = 3.196 \text{ Å}$	Hf 2g (0.0000, 0.5000, 0.5429)
						$c = 30 \text{ Å}$	N 1d (0.0000, 0.0000, 0.5000)

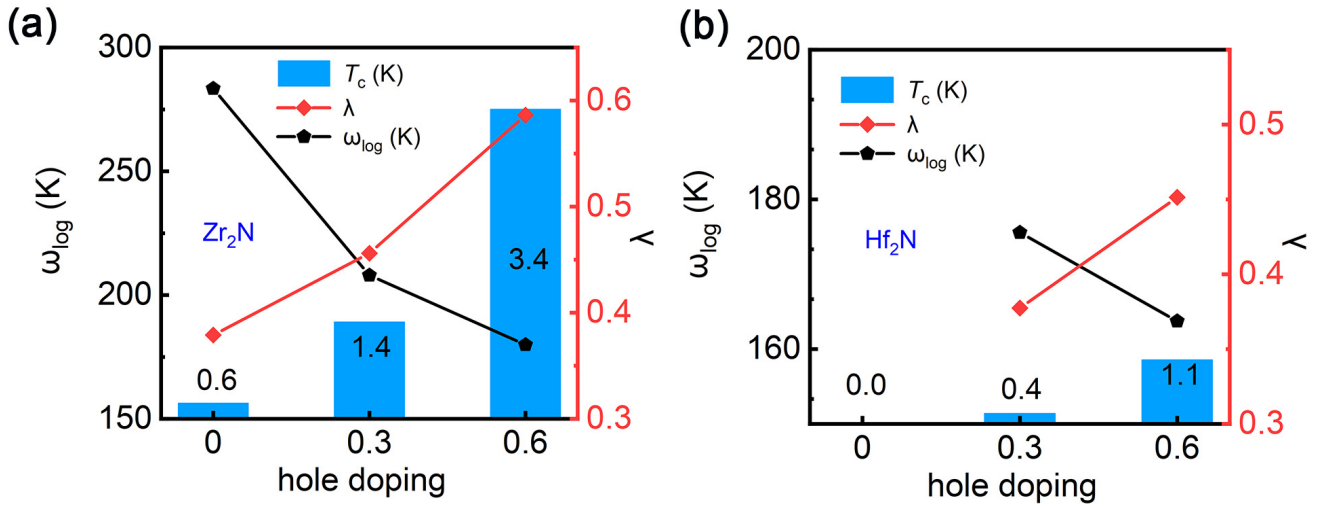


FIG. S5. Hole doping concentration (n_h) dependent T_c , ω_{\log} , and λ of the (a) Zr_2N and (b) Hf_2N monolayers.